

1 **Structure-based prediction of Ras-effector binding affinities and design of**
2 **‘branchegetic’ interface mutations**

3
4

5 Philipp Junk ^{2,3*}, Christina Kiel ^{1,2,3}

6
7 **Affiliations**

8 ¹ Department of Molecular Medicine, University of Pavia, 27100 Pavia, Italy

9 ² Systems Biology Ireland, School of Medicine, University College Dublin, Dublin 4, Ireland.

10 ³ UCD Charles Institute of Dermatology, School of Medicine, University College Dublin,
11 Dublin 4, Ireland

12

13 *Correspondence: Philipp Junk (philipp.junk@ucdconnect.ie)

14

15 **Summary**

16 Ras is a central cellular hub protein controlling multiple cell fates. How Ras interacts with a
17 variety of potential effector proteins is relatively unexplored, with only some key effectors
18 characterized in great detail. Here, we have used homology modelling based on X-ray and
19 AlphaFold templates to build structural models for 54 Ras-effectors complexes. These models
20 were used to estimate binding affinities using a supervised learning regressor. Furthermore, we
21 systematically introduced Ras ‘branch-pruning’ (or branchegetic) mutations to identify 200
22 interface mutations that affect the binding energy with at least one of the model structures. The
23 impacts of these branchegetic mutants were integrated into a mathematical model to assess the
24 potential for rewiring interactions at the Ras hub on a systems level. These findings have
25 provided a quantitative understanding of Ras-effector interfaces and their impact on systems
26 properties of a key cellular hub.

27

28 **Keywords**

29 AlphaFold, branch pruning, edgetics, enedgetics, effectors, FoldX, homology modelling, hub,
30 networks, Ras

31

32 **Introduction**

33 Ras is a key cellular signaling hub and oncogene (1). The first correct Ras structure was
34 famously described in 1989 (2) (3) and consists of the G domain super-fold (six β -strands and
35 five α -helices; (1)). It's main structural and functional characteristic is the nucleotide binding
36 site (the typical α,β -fold of nucleotide binding proteins), which can bind GTP and hydrolyze it
37 to GDP. Then, GDP gets released and a new nucleotide (favorably GTP since it is higher
38 abundant in cells) gets bound. Depending on which nucleotide is bound, the functional state of
39 RAS is different. GDP bound Ras assumes a so-called inactive conformation, whereas upon the
40 binding of GTP, the conformation of Ras is called active. The difference between the active
41 and the inactive conformation is that, in the active conformation, two loop regions called switch
42 1 and switch 2 are interacting with the GTP and thereby tightly bound to it (1) (Figure 1A).
43 This rearranges the interface of Ras in a specific way so that effector proteins with a specific
44 structural motive can interact with Ras. The structural motive required for the interaction with
45 Ras has a ubiquitin domain super-fold (4). There exist three families of these domains, called
46 Ras binding domain (RBD), Ras association domain (RA domain) and PI3K-Ras binding
47 domain (PI3K RBD) with only minor sequence and structural differences between them. In the
48 following, for the sake of simplicity, all of these will be called RBDs.

49 Ras·GTP can interact and activate many downstream effectors, some of which are better
50 studied than others (5). Well-studied effectors include PI3-kinases, RalGDS, and Raf kinases,
51 which control important cellular processes such as survival, polarization, adhesion, migration,
52 and proliferation. In our previous work, we characterized a set of 56 RBD-containing proteins
53 as potential Ras effectors, which converge into 12 classes that are linked to different
54 downstream cellular processes and phenotypes (6) (7) (8) (9).

55 Ras-effector interactions are interesting from a systems biology and network point of
56 view. Effectors use a mutually exclusive binding site on Ras, hence competition for binding
57 can occur under certain conditions (10). Also, the experimental and predicted affinities between
58 RBDs and Ras·GTP vary, ranging from nano- to micromolar K_d values (8). Previously we
59 analyzed how the amount of effectors in complex with Ras varies in different cell types (6) (7).
60 We find that only 9 effectors are predicted to bind in significant amount to Ras·GTP using the
61 RBD alone (7). However, 31 effectors are predicted to form significant complexes with Ras if
62 they are additionally recruited to the plasma membrane via other domains present in effectors
63 (piggyback mechanism, (11)). Hence, even weak binding affinities on the level of RBD-RAS
64 binding can turn into significant complex formation if effectors are recruited (e.g. in a context

65 specific manner). Thus, for systems analyses and computational models, we need good
66 estimations for all binding affinities between RBDs and Ras.

67 Structural analysis can lead to a deeper understanding of protein-protein interaction
68 (PPI). Previous we used homology modelling, based on experimentally determined complex
69 structures, to predict binding between effectors and Ras·GTP (12) (13). While this has provided
70 insights into binding propensities, a limitation of this work was that no quantitative binding
71 affinities were predicted, but qualitative binding by classifying effectors into categories of
72 ‘binding’, ‘non-binding’, and ‘twilight’. It is now timely to revisit homology modelling of Ras-
73 RBD complexes, as new template structures are available by (i) X-ray crystallography (8 of 56
74 effectors are crystallized in complex with RAS) and (ii) AlphaFold (14) (15).

75 Ras is frequently mutated in different cancers, where aberrant Ras signaling plays a role
76 in cancer initiation, progression, and metastasis via alterations in metabolism, proliferation, and
77 survival (16). As Ras cannot be directly targeted (or only certain Ras mutations) (17), much
78 hope rests on network-centric approaches (18) that involve Ras-effector interactions or
79 downstream pathways (9). Therefore, tinkering with Ras-effector binding is an attractive
80 alternative strategy for finding suitable targets for therapeutic interventions. Previously we
81 developed a ‘branch-pruning’ (or “branchegetic”, in analogy to “edgetics” (19) and
82 “enedgetics” (20)) strategy for Ras effector interactions, where mutations are introduced into
83 Ras that differentially impact binding to effectors (21). For example, introducing a mutation
84 can result in a steric clash in the interface formed with one effector, but not with another; hence
85 the interaction with one effector is broken while intact for another.

86 In this work, we first generate homology models of all Ras-effector (RBD) interactions
87 and predict affinities of the RBDs in complex with Ras·GTP. We then use the generated model
88 structures to employ a systematic branchegetic strategy that explores the impact of Ras interface
89 mutants on binding to all effectors. Altogether, our results contribute to a quantitative and
90 systems-level understanding of Ras-effector interactions and further our understanding of Ras
91 in health and disease.

92

93

94 **Results**

95 **Structural analysis of experimental complex structures**

96 From the few experimentally determined complex structures of Ras with these RBDs, there are
97 some structural similarities that can be determined. The main interface on the site of Ras
98 consists of the two switch regions, switch 1 and switch 2. One of the main structural features

99 of the interface between Ras and RBDs is the formation of an intra-molecular β -sheet between
100 $\beta 2$ on RAS and $\beta 2$ on the RBD. This interaction is a highly conserved structural feature across
101 all available complex structures, with deviations in orientation of less than 1 Å (Figure 1B, see
102 Methods for MAE).

103 Analyzing the energetic profile of the interface *in silico* using the FoldX force field
104 shows that there are also some recurring hotspots in the interface (highlighted in Figure 1C).
105 I36, D38 and Y40 are well characterized as important residues for the interaction between Ras
106 and effector domains. Additionally, for the structures 3DDC and 1LFD, the mutation E31K was
107 introduced to stabilize the complex for crystallization. Our analysis confirms that this interface
108 mutation has indeed been favorable for the complex formation. Finally, the energetic
109 contributions of the function regions switch 1 and 2 to the interface were analyzed. Both relative
110 and absolute contributions are diverse, although switch 1 contributions to binding dominate
111 (Figure 1D). Altogether, the analysis of existing Ras-RBD effector structures indicates that
112 although there are many common features of the Ras RBD interface such as the intra-molecular
113 β -sheet or the hydrophobic patch around I36, the actual energetic contributions can come from
114 different parts of the interface. It also sets the basis for a successful homology modelling
115 approach.

116

117 **Homology modelling and characterization of modelled interfaces**

118 In order to study these interface features in a more diverse set of structures, homology models
119 of the complex between RAS and RBD were constructed for all proteins containing an RBD in
120 the human proteome.

121 The homology modelling pipeline is based on the already existing complex models
122 (Table S1). Also, with the recent release of AlphaFold2 (14) and the accompanying AlphaFold
123 Protein Structure Database (15), the RBD domains of all potential effectors were extracted from
124 that database and used. The structures of RBDs are predicted with good confidence by
125 AlphaFold2 and our analysis indicates that AlphaFold2 is reliable at predicting the RBD fold
126 (Figure S1). Additionally, AlphaFold2 complex modelling was attempted for all potential
127 complex structures and models which AlphaFold2 were confident in (by Predicted Alignment
128 Error (PAE)) and where the β -sheet alignment of the interface was within a tolerance to what
129 has been observed in crystal structures, were used as templates as well (Figure S2 and S3,
130 compare MAE Figure 1). There are two kinds of templates to use: 1) complex templates which
131 comprised of the already experimentally determined complex structures of Ras and RBDs, as
132 well as “good” AlphaFold2 predicted complex templates (Table S1), and 2) templates of the

133 RBDs alone which were extracted from the AlphaFold2 EMBL database (Table S2). An
134 overview over the pipeline is depicted in Figure 2. Homology modelling was performed using
135 homelette (22) with modeller and altMod. Evaluation of predicted structures was performed
136 using QMEAN, MolProbity and SOAP potentials. The top 300 models for each target for each
137 source of complex templates (experimental or AlphaFold2) were selected by combined score
138 and FoldX analysis (interaction energy and alanine scan) was performed.

139 In order to evaluate our approach, we generated a validation set, in which we created
140 models for the structures already solved by X-ray crystallography without using information
141 from the specific structure. Models generated in this validation set were compared to the
142 underlying ground truth by assessing their correlation of the *in silico* alanine scan results to
143 those of the crystal structures of interest. Using this ground truth, different methods to select
144 representative models from the hundreds of structures were assessed. In particular, we evaluated
145 the hyperparameters of an unsupervised learning pipeline comprised of different feature
146 selection and dimensionality reduction strategies followed by clustering with the OPTICS
147 algorithm (see Methods for more details about the hyperparameter space). After clustering,
148 three representative structures were chosen. Based on the performance in the validation set, the
149 optimal set of hyperparameters was chosen (Table S3, see Figures S4 and S5). The described
150 strategy for identifying representative structures was then applied to all target complexes and
151 we ended up with three representative complex structures for each effector.

152 Analogous to how we characterized the interfaces of the experimentally determined
153 complex structures before, we performed the same analysis on the complex models. The overall
154 FoldX interaction energies for the models are diverse, indicating that maybe some of the
155 complexes are energetically unfavorable and would not form (Figure S6B). In general, the
156 binding energies are lower than what would be observed in crystal structures, which is to be
157 expected. There are one or two outliers with regards to FoldX binding energy, namely RASSF8
158 and PIK3C2B. In particular, RASSF8 is also showing an uncommon hotspot profile, with
159 multiple unfavorable hotspots that are only appearing for this set of structures (Figure S6A).
160 Based on this behavior, RASSF8 is excluded from further analysis.

161 The analysis of hotspots confirmed the already established hotspots. I36, Y40, D38 and
162 E37 are the most commonly observed hotspots (Figure 3A, Figure S6A). Interestingly, while
163 I36, Y40, and E37 are exclusively favorable to the interaction with the effector protein, D38
164 seems to be also unfavorable in some of the structures (Figure 3B). The energetic diversity of
165 the hotspot D38 was further investigated in the models. For this, two models were picked for
166 which D38 was a favorable hotspot in the alanine scan analysis (Figure 3C: RASSF1, Figure

167 3D: RGL3), and two models were picked for which it was unfavorable (Figure 3E: ARAP2,
168 Figure 3F: RAPGEF3). Next, neighboring amino acids were analyzed. For favorable
169 interactions, we were able to observe positively charged amino acids. On RASSF1, we find
170 K216 and H217, whereas on RGL3, there is R630. These amino acids probably form strong
171 interactions with the negatively charged D38 on Ras. In contrast, for the models where D38
172 comes up as an unfavorable hotspot in the interface, we observe an uncharged, mostly
173 hydrophobic neighborhood.

174

175 **Estimation of binding energies**

176 One of the applications of the structural models that were generated was to use them for the
177 estimation of binding energies. Since experiments measuring the binding energy between two
178 proteins are experimentally very challenging and error-prone (23), we were implementing an *in*
179 *silico* approach. Also, while FoldX is good at predicting energy changes to interaction energy
180 or protein stability on mutation, the absolute interaction energies for protein complexes usually
181 are not well correlated with experimental values (24). Because of this, a supervised learning
182 regression pipeline was built based on features extracted from the modelled structures and a
183 collection of experimentally determined binding energies of different Ras-effector complexes
184 (Table S5). From a combination of different regressors, feature extraction procedures, and
185 hyperparameters, the best approach was determined using a cross validation strategy (see
186 methods). A support vector machine-based regressor (see hyperparameters in Table 4)
187 performed best in cross-validation with an R2 score of 0.53. Then, the performance of the best
188 approach was evaluated in an out-of-sample test set, where it achieved an R2 score of 0.77. The
189 model was then used to predict the interaction energies for the complexes without prior
190 experimental measurements (Figure 4, Table S5). The predicted binding affinities for our
191 models range 4 orders of magnitude, between the highest predicted affinity for BRAF of 0.02
192 μM to PIK3C2B with the lowest predicted affinity of 588 μM . The highest binding effectors
193 are quite well characterized (RAF family, PI3K, RASSF5, RIN1, RalGDS, AFDN (8)). As
194 experimental measurements of the PI3K family members are difficult as the RBD is not easy
195 to express and purify in isolation, it is noteworthy that we assign three of the good binding
196 affinities to PI3K family members (PIK3CA, PIK3CD, PIK3CG). A big group of effectors has
197 affinities in the range of 1 to 10 μM . For example, RASIP1 was previously in the “likely no
198 binding” category (8), and is now predicted to have an affinity in complex with Ras of 2.7 μM .
199 RAPGEF5 and RGL3 were previously in the “unknown” (8) category and have predicted
200 affinities of 9.2 and 5.6 μM , respectively. Another big group of effectors has affinities in the

201 range of 10 to 100 μM . Especially the first one could be interesting for modulation of binding
202 affinity by the piggy back mechanism (7).

203

204 **Switch contributions to binding**

205 Having Ras-effector structural models available allowed us to analyze the individual
206 contributions of switch 1 and switch 2 to binding using the results from alanine scanning
207 (similarly as done before for the X-ray Ras-effector structures). We find that generally most
208 structures are dominated by favorable switch 1 contributions (Figure 5 and Figure S7). Switch
209 2 contributions are surprisingly small. We also predict more contributions from regions outside
210 switch 1 and switch 2 as in the X-ray structures. For the two weak affinity binding groups (10
211 μM ($K_d < 100 \mu\text{M}$ and ($K_d > 100 \mu\text{M}$) switch 1 contributions are in the range of 4 to 5 kcal/mol
212 with small (~ 1 kcal/mol) contributions from switch 2 and remaining parts involved in interface
213 formation. For the two strong affinity groups ($K_d < 1 \mu\text{M}$ and $1 \mu\text{M}$ ($K_d < 10 \mu\text{M}$) switch 1
214 contributions increase to 6 to 9 kcal mol with also increasing switch 2 contributions (1 to 2
215 kcal/mol). We also observed negative switch contributions (mainly for switch 1), indicating
216 that these proteins are either not well predicted or non-binders. Indeed, all structures with
217 negative switch energies are weak binders.

218

219 **Branch pruning analysis using Ras-effector model structures**

220 Next, we were interested in exploring surface mutations on Ras that would selectively influence
221 the binding to some, but not all effectors. Both enhancing and inhibiting mutations are of
222 interest. This could enable the engineering of the Ras effector system to respond to stimuli in
223 different ways and to study selective sets of effectors. We previously reported a framework for
224 the identification and evaluation of so called ‘branch pruning’ mutations (21). Since our protein
225 is interacting with a many different effectors at the same time through the same interface it will
226 be quite unlikely to identify mutations that selectively target only one protein. Instead, it is more
227 likely that we will identify mutations that enhance in interaction with some proteins while
228 inhibiting some others.

229 Figure 6 shows a heatmap of all identified mutations of interest and their effect on all
230 effectors. Some interesting mutations to highlight are mutations around I36, that are almost
231 exclusively unfavorable while affecting almost every structure. D37 mutation are more
232 selective and also exclusively disruptive. D38 is mixed, as our analysis of the hotspot already
233 indicates. This is probably the best point to disrupt the system. Y40, interestingly, while being
234 a ubiquitous hotspot, is not a good spot for engineering the interface because mutations seem

235 to affect protein stability (compare with Figure S8A). Also of interest is that we detect both
236 mutations that increase and disrupt binding (Figure S8B).

237

238 **Assessment of rewiring of Ras-effector interaction on a systems level**

239 Finally, we want to evaluate the behavior of the Ras effector system based on our predicted
240 binding energies and based on the introduction of different branch pruning mutations. For this
241 means, we went back to our mathematical model of the Ras-effector system that incorporated
242 affinities and high-quality proteomics data in 29 human tissues (7). Here, all 29 tissue systems
243 were simulated at 20% and 90% GTP load on Ras. We are using exclusively the predicted
244 binding energies for this (except RASSF8, see methods). Overall, the results for the systems
245 without a branch pruning mutation are comparable to previous findings (Figure 7A; (7)). The
246 Raf family members ARAF, BRAF and RAF1 dominate the binding profile in complex with
247 Ras. Other effectors that are in high amount in complex with Ras in at least one of the 29 tissues
248 are RGL2, RASSF7, RASSF5, RASIP1, RALGDS, PIK3CD, PIK3CA, and AFDN.

249 Expanding on this, we introduced our branch pruning mutations to the mathematical
250 model. In total, there are 200 interface mutations that do not significantly affect overall protein
251 stability but affect binding to at least one of the effectors. Some of the branch pruning mutations
252 are able to dramatically change the system in all tissues, as can be seen from the example of
253 D38A (Figure 7B). With a single interface mutation, almost all RAF binding is quenched, and
254 other effectors start to compete for the binding. Interestingly, which effectors come up depends
255 on the tissue.

256 Next, we wanted to explore whether there are recurring states that the modelled system
257 assumes and whether these states are dependent on Ras-GTP load, the tissue, or interface
258 mutation. To this end, we applied uniform manifold approximation and projection (UMAP) to
259 our systems to transform a high-dimensional space of absolute and relative effector binding into
260 a 2D space. Then, we used OPTICS to identify areas of high density in this 2D plane and
261 assigned them into 19 distinct clusters (Figure 7C). For each cluster, we picked three of the
262 systems at random and visualized their relative effector binding (Figure S9). Each of these
263 clusters belongs to a different “state” that the Ras-effector system can be rewired into, with
264 systems belonging to a specific state showing similar trends in effector binding. Many of the
265 systems are dominated by ARAF binding, as it would be expected, but even for these there are
266 differences in the secondary effectors. To understand what the attributes of different “states” of
267 the systems are, two of them were picked and investigated for Ras-GTP load, tissue
268 composition, and interface mutation status (Figure 7DE). We find that there are different ways

269 a distinct state of the system can come together: for the state analyzed in Figure 7D, we can see
270 that it is composed of many different tissues, but only a handful of interface mutations, most of
271 them D38 mutations. This indicates that this state can be reached from many different tissues
272 by a specific, recurring set of mutations. In contrast, the state analyzed in Figure 7E is entirely
273 composed of a single tissue (lymph node) with many different mutations, indicated that this
274 state can only be reached by a specific tissue. Interestingly, both states analyzed are diverse in
275 terms of Ras-GTP load. To conclude, we identify 19 distinct states of the Ras-effector systems
276 and show that there are different mechanisms on how these states are formed.

277 Finally, we wanted to explore to which extend, for a specific effector, it is possible to
278 modulate its binding. For this, we visualized the possible changes to the relative amount of
279 effector bound to Ras across all systems tested (Figure S10). On the side of proteins that can be
280 negatively influenced, mostly the high-affinity binders such as RAF family proteins show up,
281 which is to be expected. Some effectors cannot be influenced by the branch pruning mutations,
282 either because they are energetically not affected or because their concentrations in any of the
283 29 tissues do not leave them in a position to compete for binding. Examples for this would be
284 RADIL or the TIAM family proteins. The effectors with the highest propensity to have their
285 binding enhanced are AFDN, RADIL, SNX27, RASSF5. In summary, based on a large set of
286 Ras-effector models, we predicted Ras branchetic mutations and evaluate their binding in a
287 tissue-specific Ras competition model. The Ras mutations, once introduced into cells or tissues,
288 can be used as a tool to probe the contribution of specific effector pathways to an output or
289 cellular phenotype.

290

291

292 **Discussion**

293 In this work we have shown a complete structural reconstruction of Ras and the RBDs of its
294 effectors based on state-of-the-art technology. We used these structural models to investigate
295 the workings of the interface between Ras and its effectors, as well as to search for and identify
296 potential branch pruning mutations on Ras that would alter the behavior of the underlying
297 system. We analyzed the effects on the steady state of the Ras effector system.

298 Recent advances in structural modelling, mostly by the development and release of
299 AlphaFold2 and similar algorithms have pushed the field of structural bioinformatics forward.
300 This development was crucial for the quality of this study. While a normal homology modelling
301 pipeline would have been successful, the inclusion of both aspects of AlphaFold2 models was
302 essential for the quality of the results. On the one hand, finding additional potential complex

303 templates diversified the possible configurations of the interface that we could use to generate
304 our models. On the other hand, having high quality templates of the RBDs enabled us to
305 improve the structural predictions. Interestingly, with all the advancements that AlphaFold2
306 brought, this combined AlphaFold2/homology modelling approach yielded more consistent and
307 better results for this particular question.

308 There is a growing body of literature about how Ras dimerizes or forms multimers, or
309 interacts with the membrane to modulate the signaling. All these aspects have been deliberately
310 left out for this approach. The essence of the interaction of Ras and its effectors is the binary
311 protein-protein interaction between the Ras switch regions and the RBD. This common feature
312 was the focus of this work, and we believe that other factors such as dimer/multimerization of
313 Ras, the composition of the membrane, etc., are only modulators for this interaction.

314 By creating a complete structural system, we were able to investigate and understand
315 the interactions of Ras with its effector molecules on a different level. Crucially, it enabled us
316 to analyze how *in silico* mutations of the system could affect its behavior. This is an interesting
317 approach for a lot of different systems, not just the Ras effector system. However, there are
318 certainly challenges. The prediction and verification of a protein-protein interface can be very
319 complicated, and the techniques for modelling protein-protein interactions are not sufficiently
320 developed to easily translate that approach to a larger scale. Probably the main reason why it
321 was possible to construct this structural system for the Ras-effector system was because it is a
322 conserved domain-domain interaction between homologue proteins. Although the sequence
323 identity of the RBD sequences is not well preserved anymore, the structural fold of these
324 domains has been preserved. Additionally, there is also the preserved mode of binding by the
325 formation of the intermolecular β -sheet. These factors were favorable for the construction of
326 the structural system and would need to be addressed if this approach were to be taken to a
327 higher scale. Recent publications are already able to work on system-wide structural prediction
328 for interactions (25). These approaches are very promising for the structural characterization of
329 known protein complexes and can identify high-confidence novel interactions as well.
330 However, for the exhaustive characterization of a full system, especially with transient
331 interactions, the distinction between true and false positives seems to remain challenging.

332 Finally, we hope that our structural and systems analysis of the branch pruning interface
333 mutations will enable interesting experimental setups that study different downstream pathways
334 from Ras. Some of the more promising candidates are AFDN, RADIL, SNX27, RASSF5. The
335 downstream pathways of Ras that are best characterized are the RAF-MEK-ERK signaling
336 pathway and the PI3K-AKT signaling pathway. However, some of the other proteins might

337 play a role in a physiological or pathophysiological context as well. AFDN is essential for the
338 organization of adhesion between cells (26), function that is often impaired in cancer (27).
339 RADIL is also linked to cell adhesion, and recent data showed that knockdown of was linked
340 to decreased cell proliferation and invasion (28). SNX27 is also part of signaling pathways that
341 link to cell adhesion and barrier function (29). RASSF5 is a tumor suppressor and has been
342 shown to inhibit growth and invasion and to induce apoptosis (30). Importantly, all branchegetic
343 mutations were studied on a systems level using a tissues specific Ras competition model. These
344 models can easily be adapted for specific cell systems of interest, provided that estimates for
345 Ras and effector abundances are available. Altogether, this work contributed to a quantitative
346 understanding of a key cellular hub protein – Ras.

347

348

349 **STAR★Methods**

350 Detailed methods are provided in the online version of this paper and include the following:

- 351 • **KEY RESOURCE TABLE**
- 352 • **RESOURCE AVAILABILITY**

353

354 **Lead contact**

355 Further information and requests for resources should be directed to Philipp Junk
356 (philipp.junk@ucdconnect.ie)

357

358 **Code availability**

359 The code will soon be deposited on Zenodo.

360

361 **METHOD DETAILS**

362 **Experimentally determined Ras-effector complex structures**

363 Structures were downloaded from the PDB. In the case where multiple models were available,
364 the best one by MolProbity score was selected (31) (32). The PDB files were processed so that
365 all GTP and Mg²⁺ annotations were in the expected format. The list of used template structures
366 can be found in Table S1.

367

368 **Interface characterization**

369 Hotspots residues were determined by FoldX *in silico* Alanine scan (33) (24) (20) (34) (35). In
370 detail, each residue on both RAS and the effector was mutated to alanine and the *in silico* change
371 of binding energy $\Delta\Delta G$ was determined as such:

$$372 \quad \Delta\Delta G_{\text{alascan}} = \Delta G(\text{mut}) - \Delta G(\text{wt})$$

373 A positive $\Delta\Delta G$ value indicates that the mutated residue is involved favorably in the interaction,
374 whereas a negative $\Delta\Delta G$ value indicates that the mutation to alanine improved the interaction
375 between the two proteins. The standard error for $\Delta\Delta G$ values in FoldX is around ± 0.8 kcal/mol.
376 In order to identify the most important residues for the respective interaction, a $\Delta\Delta G$ cut-off of
377 1.6 kcal/mol was chosen for the investigation of crystal structures. Since the energies are
378 systematically lower in the modelled complex structures, a cut-off of 1.2 kcal/mol was chosen
379 for those.

380 Based on the alanine scan results, the contribution of the two major functional regions
381 in the RAS interface (36), switch 1 (residues 20-42) and switch 2 (residues 56-76) to the
382 interaction were determined. For each functional region and the remainder of Ras, the $\Delta\Delta G$
383 values were filtered by $\text{abs}(\Delta\Delta G) > 0.8$ kcal/mol and then summed up. The definition of the
384 switch regions used here is more generous than what is normally used in the literature, and it
385 would be probably more correct to label them as “switch-influenced” regions. These residue
386 ranges aim to capture the regions in the interface that are affected by the movement of switch
387 1 and 2 during the transition from the inactive GDP bound state to the active GTP bound state.
388 The conserved intra-molecular β -sheet between the $\beta 2$ sheet on Ras with the $\beta 2$ sheet on the
389 effector is evaluated by measuring the differences in inter-molecular distances between the β
390 sheets in the experimentally solved complex structures and comparing them to the ones in a
391 structure of interest. This measurement has been named Measured Alignment Error (MAE) in
392 this manuscript:

$$393 \quad MAE(\text{res}_{\text{eff}}, \text{res}_{\text{ras}}) = \frac{\sum_{i=1}^n \sqrt{(\text{dist}_{\text{model}} - \text{dist}_{\text{ref}})^2}}{n}$$

394 with $\text{dist}_{\text{model}}$ being the Euclidean distance between two residues in the model of interest;
395 dist_{ref} being the Euclidean distance between the residue on Ras and the corresponding residue
396 in the reference structure, as determined by structural alignment using TMalign (37); and n
397 being the number of reference structures. The references used were the X-ray complex
398 templates found in the PDB (Table S1). When the MAE is calculated for X-ray complex
399 templates, the comparison with itself is removed from the calculation.

400

401

402 **AlphaFold2 determined single structures for RBDs**

403 For each protein containing one or more potential RBD sequences as identified in (6), the full
404 structure was obtained from the AlphaFold Protein Structure database (14) (15) (Release 1,
405 accessed September 2021). The sequences of the RBDs were obtained from Pfam (38) and
406 UNIPROT (39). The part of the structures that correspond to RBD sequences was subsequently
407 extracted from the AlphaFold2 structures. The list of used templates as well as information
408 about the extracted RBD domains can be found in Table S2.

409

410 **AlphaFold2 determined complex structures: generation and selection**

411 AlphaFold2-multimer/ColabFold (version 1.3.0) was run on a local computer (40) (14) (41).
412 Multiple sequence alignments were generated from MS2seq (42) (43) (44) (45). Complex
413 models were generated with HRAS as interaction partner. For each target, five models were
414 generated with additional template search and five without additional template search (40) (46).
415 The resulting model were relaxed as per ColabFold defaults (40) (47). For each model, several
416 metrics were evaluated. Firstly, AlphaFold2's Predicted Alignment Error (PAE) was taken
417 into consideration. PAE is an estimation of the error of pairwise distances between residues,
418 that can be used to assess how confident AlphaFold2 is in the inter-domain arrangement of its
419 models. Secondly, FoldX (33) (24) (34) (35) interaction energies were determined for the
420 complexes as described above. Finally, the expected orientation of the inter-molecular β sheets
421 was evaluated by MAE. The best model by MAE was selected for each target, and then all
422 complex structures with a MAE > 1Å were removed.

423

424 **Homology modelling pipeline**

425 Alignment generation, model generation and model evaluation were performed using the
426 homelette homology modelling interface (22). Inputs to the homology modelling pipeline were
427 complex structures of Ras in complex with some effectors, either experimentally determined or
428 selected from AlphaFold2 complex predictions, as well as AlphaFold2 models of all RBDs of
429 interest. For each target, all combinations of the RBD template with all complex templates were
430 used to generate 300 models of the target in complex with HRAS each. The different sources
431 for the complex templates were run separately with slight differences in the modelling
432 procedure. For complex templates of experimental origin, TMalign (37) was used to generate a
433 structure-based sequence alignment based on the RBD in the complex template and the single
434 RBD of the target structure. Then, with those two templates as inputs, models were generated.

435 For complex templates of *in silico* origin, structure-based sequence alignments were generated
436 with TMalign (37) as described. As an additional template a HRAS single structure (5P21 (3))
437 was used in the modelling process since the AlphaFold2-generated complex templates, in
438 contrast to the complex templates of experimental origin, do not have information about the
439 important heteroatoms GTP and MG2+ in the Ras part of the structure. Models were generated
440 using modeller (48) (49) with the altMOD extension (50). All models generated were evaluated
441 using QMEAN (51) (52), MolProbity, (31) (32) and SOAP (53) potentials. A combined score
442 was determined based on borda count as such:

443
$$combined\ score(X) = \sum_{i=1}^m n - rank_i(X)$$

444 For an observation X with $i \dots m$ being a collection of evaluation criteria and n the total number
445 of observations. A structure with high borda score is a structure that performs well across all
446 metrics.

447 For each of the different sources of complex templates (experimental or *in silico*), 300 models
448 were selected in a first selection step based on the combined score. These 600 models per target
449 were then further analyzed using FoldX. *In silico* interaction energies were determined and *in*
450 *silico* alanine scan was performed (see Interface Characterization).

451 In addition to generating models for unknown targets, a set of validation models based
452 on the experimentally solved models were generated as well. For each of the seven PDB
453 complex structures, 300 models were generated. Inputs were restricted so that the structure to
454 be modelled would not be used as a complex template, but only the remaining six
455 experimentally derived complex templates. For each validation target, 300 models were
456 selected as described above.

457 Using the results from the analysis with FoldX, representative structures were selected
458 based on an unsupervised learning workflow. As the clustering algorithm of choice, Ordering
459 Points To Identify the Clustering Structure (OPTICS) (54) was used, as implemented in scikit-
460 learn (<https://jmlr.csail.mit.edu/papers/v12/pedregosa11a.html>). OPTICS is a density-based
461 clustering method, which unlike the more popular k-means clustering does not require a
462 manually set input of the number of clusters. Additionally, OPTICS is able to label data points
463 as outliers. Several approaches to feature selection and/or feature engineering, hyperparameters
464 of OPTICS, as well as methods for selecting representative structures from clusters were
465 evaluated against the set of validation models (Table 3). To select the best combination of
466 hyperparameters, for each combination, the *in silico* alanine scan results of the representative
467 structures were correlated to the results of corresponding PDB structures, and the combination

468 of hyperparameters with the most stable performance across all validation sets (by minimum z-
469 score of the correlation against the PDB structure for all 7 validation sets) was chosen. The best
470 combination of hyperparameters is highlighted in (Table 3).

471

472 **Estimation of binding energies**

473 Supervised learning based on a number of FoldX-derived features was used in order to estimate
474 binding energy of complex models. The features consisted of the FoldX interaction energy, the
475 energy contribution of switch 1, 2 and the remainder of the Ras protein interface (see Interface
476 characterization), and the $\Delta\Delta G$ values for hotspot residues on Ras (cut off 1.2 kcal/mol). All
477 features were standardized and highly intercorrelated features were removed. Data preparation
478 was performed in R.

479 The experimental measurements of the dissociation constant between Ras-effector
480 complexes were collected from several publications (see Table S5, also available as
481 supplementary data). Effectors that were experimentally determined as non-binders were
482 removed from the data set due to uncertainty how to encode them with the varying technical
483 limitations on detectable binding energies at the time of their publication. Also, the models
484 generated for RASSF3 seem to be outliers with regards to FoldX interaction energy (see figure
485 7) and were therefore removed from the prediction. A test set was manually chosen from the
486 available experimental measurements to cover the full spectrum of experimentally determined
487 interaction energies. At the end, this gave us a training set with 51 observations (17 * 3 models)
488 and a testing set with 12 observations (4 * 3 models).

489 Supervised learning was performed in scikit-learn
490 (<https://jmlr.csail.mit.edu/papers/v12/pedregosa11a.html>) using different combinations of
491 feature selection algorithms and regressors. Feature selection was performed using either f-
492 regression or mutual information as implemented by scikit-learn. Regression was evaluated for
493 different algorithms with various hyperparameter spaces (see Table S4). All combination of
494 feature selection and regression were evaluated using Group-K-Fold cross validation within the
495 training data, with k=5 and the groups corresponding to the three structural models chosen for
496 each target. Models were evaluated using R2 score. The best performing combination was
497 trained on the whole training data and evaluated against the test data. Finally, this model was
498 used to predict the binding energies for the complex structures without experimental data.

499

500 **Branch pruning**

501 FoldX was used to evaluate the effect of interface mutation on the binding energies in the
502 modelled complex structures. As previously described, (21) the FoldX command PSSM was
503 used to evaluate the changes in binding energy, and the FoldX command PosScan was used to
504 evaluate if mutations impacted the stability of RAS.

505 All mutations that were destabilizing HRAS in either of two structures (3TGP and 5P21)
506 were removed from the analysis (cutoff 1.6 kcal/mol). Then, between the three models for each
507 target structures, it was checked if a mutation had a noticeable impact ($> \pm 1$ kcal/mol) in at
508 least two of the three structures. If so, the changes in binding energy for all models above/below
509 the cutoff were averaged.

510

511 **Systems analysis**

512 A mathematical model of the Ras-effector system was set up as previously described (6) (7).
513 The model is based on classic ligand-receptor kinetics according to the assumption of
514 conservation of mass. A system of ordinary differential equations was set up and steady states
515 were calculated as described. The reactions are expressed as such:

516 $R + E_i \xrightleftharpoons{(k_i, k_{-i})} RE_i$ With R representing the molar concentration of Ras, E_i the molar
517 concentration of an effector of the set of $i \in (1, 2, \dots, 54)$ effectors (all modelled proteins,
518 except for proteins from the Ubiquitin family) and RE_i the molar concentration of a Ras-effector
519 complexes. The complex is formed at rate k_i and dismantled at rate k_{-i} . These rates define the
520 dissociation constant:

$$521 \quad K_{d_i} = \frac{k_{-i}}{k_i}$$

522 Due to the assumption of mass conservation,

$$523 \quad R_{tot} = R + \sum_1^{54} RE_i$$

524 and

$$525 \quad E_{tot_i} = E_i + RE_i$$

526 the system to solve therefore is:

$$527 \quad R_{tot} = R + \sum_1^{54} RE_i$$

$$528 \quad E_{tot_i} = E_i + RE_i$$

$$529 \quad K_{d_i} = \frac{(R * E_i)}{RE_i}$$

530 For the set of $i = \{1,2, \dots, 54\}$ and can be numerically solved for RE_i . The system was solved
531 using SciPy.

532 The concentrations for the species in the model were taken from the supplementary data
533 of (7), in which molar concentrations were derived from high-quality proteomics data set of 29
534 different human tissues (55). The concentration of Ras proteins (HRAS, NRAS, KRAS) were
535 pooled together and then multiplied with a loading factor to take into account the balance
536 between active (GTP bound) and inactive (GDP bound) Ras. This loading factor was set to 0.2
537 for a normal RAS system, and 0.9 for a system hyperactivated by an oncogenic hotspot
538 mutation.

539 The binding affinities were taken from the predicted binding affinities (see Estimation
540 of binding affinities), with the exception of RASSF3 for which we are not confident in our
541 structural predictions. An experimentally determined binding affinity for RASSF3 was
542 substituted from (56). Additional sets of binding affinities based on the branch pruning analysis
543 were evaluated as well. For this, the predicted binding affinities were adapted by the ddG values
544 from the branch pruning analysis. For the case that a system with hyperactivated Ras was
545 considered, it was made sure that common oncogenic hotspots such as G12, G13 and Q61 do
546 not influence the binding energies for any effector.

547 Some sets of parameters were not solvable in a physically meaningful solution space
548 (negative concentrations) or at all, these parameter sets were removed from further analysis.

549 To gain an overview over all solved system, absolute and relative effector bindings were
550 transformed using UMAP (57) and visualized. OPTICS clustering (54) was performed on the
551 UMAP transformed data (parameters: min_sample = 25, min_cluster_size=200).

552

553 **Data analysis and visualization**

554 All data analysis, unless otherwise noted was performed in R using the tidyverse environment
555 (<https://www.R-project.org/>). Visualizations were generated using ggplot2 (H. Wickham.
556 ggplot2: Elegant Graphics for Data Analysis. Springer-Verlag New York, 2016.).
557 Visualizations of protein structures were generated using PyMol (version 2.5.0)
558 (<https://pymol.org/2/support.html>).

559

560 **Figure legends**

561 **Figure 1. Noticeable features of the Ras-RBD interfaces**

562 (A) Overview of interface features for the Ras-RAF1 interface. Highlighted are the
563 intramolecular β -sheet alignment, the assembly of the Ras interface by the switch regions and
564 energetic hotspots in the interface.

565 (B) β -sheet alignment for experimentally determined complexes (MAE). A lower value
566 indicates a more similar alignment of the intramolecular β -sheets compared to other crystal
567 structures.

568 (C) FoldX alanine scan hotspots on RAS for experimentally determined complex structures.
569 The color scale is confined to the limits [-1.6, 1.6]. Positive $\Delta\Delta G$ values indicate a loss in
570 binding energy upon mutation, which reflects that the respective amino acid contributes to
571 binding.

572 (D) Energetic contributions of functional regions based on alanine scan analysis.

573

574 **Figure 2. Overview over the homology modelling pipeline**

575 The principal homology modelling steps are shown from left to right with the steps of “Target
576 Identification”, “Template Identification”, “Alignment Generation”, “Complex Model
577 Generation”, “Evaluation & Selection 1”, and “Evaluation & Selection 2”. In the “Validation”
578 process, the homology modelling pipeline is run on a set of 7 RBD domains from known x-ray
579 structures. The “Production” process describes the generation of 61 domains (RBD and
580 Ubiquitin super-fold domains as controls).

581

582 **Figure 3. Energy hotspots in modelled structures**

583 (A) Heatmap of FoldX alanine scan averaged from the three representative structures on each
584 target. The color scale is confined to the limits [-1.6, 1.6]. Hotspot residues with a $\Delta\Delta G \geq 1.2$
585 or ≤ -1.2 kcal/mol were marked.

586 C-F) Local neighborhood of D38 in structures where D38 is a favorable hotspot (C: RASSF1,
587 D: RGL3) or an unfavorable hotspot (E: ARAP2, F: RAPGEF3). Ras and the effector structures
588 are visualized in blue and green, respectively. Polar interactions between charged amino acids
589 are indicated with dashes.

590

591 **Figure 4. Results of the affinity prediction for all Ras-effector complex structures**

592 Visualization of predicted binding affinities. The three representative structures for each target
593 are visualized as black dots, with the averaged affinity (based on averaged energy) is visualized
594 as a red cross.

595

596 **Figure 5. Switch contributions for the summed-up energy contributions grouped by their**
597 **predicted binding affinity**

598 (A) Energy contributions were separately calculated for switch 1 switch or the rest of the Ras
599 interface by summing up energy energies from the *in silico* alanine scan analysis. Complexes
600 were grouped based on their predicted binding affinities into four groups.

601 (B – E) Examples of the switch contributions for each of the four groups. Visualized are BRAF
602 (panel B), AFDN_1 (panel C), ARHGAP20 (panel D), and PIK3C2B (panel E).

603

604

605 **Figure 6. Energetic characterization of RAS interface mutations that affect effector**
606 **binding**

607 The color scale is confined to the limits [-3.2, 3.2]. Hotspot residues with a $\Delta\Delta G \geq 1$ or ≤ -1
608 were marked.

609

610 **Figure 7. Ras-effector interaction rewiring at a systems level**

611 (A-B) Effects of interface mutation on the Ras-effector system. Heatmap of effectors bound to
612 Ras at 20% Ras-GTP load in 29 tissues in (panel A) WT interface and in (panel B) with the
613 effects of a D38A mutation.

614 (C-E) Overview over the possible states the Ras-effector system can assume. UMAP
615 transformation of all simulated systems. Similar systems were identified using OPTICS
616 clustering (panel C). 19 identified clusters are colored in rainbow colors, with systems classified
617 as outliers colored in grey. Characterization of two identified state clusters in terms of Ras-GTP
618 load, tissues, interface mutations, and most representative effectors (panels D and E). For the
619 tissue and mutation pie charts, all groups that were smaller than 5% of the total observations
620 were collapsed into the “Other” group.

621

622

623

624 (C) UMAP transformation of all simulated systems. Similar systems were identified using
625 OPTICS clustering. 19 identified clusters are colored in rainbow colors, with systems classified
626 as outliers colored in grey.

627 (D) and (E) Characterization of two identified state clusters in terms of Ras-GTP load, tissues,
628 interface mutations, and most representative effectors. For the tissue and mutation pie charts,
629 all groups that were smaller than 5% of the total observations were collapsed into the “Other”
630 group.

631

632

633

634

635

636

637

638

639

640

641

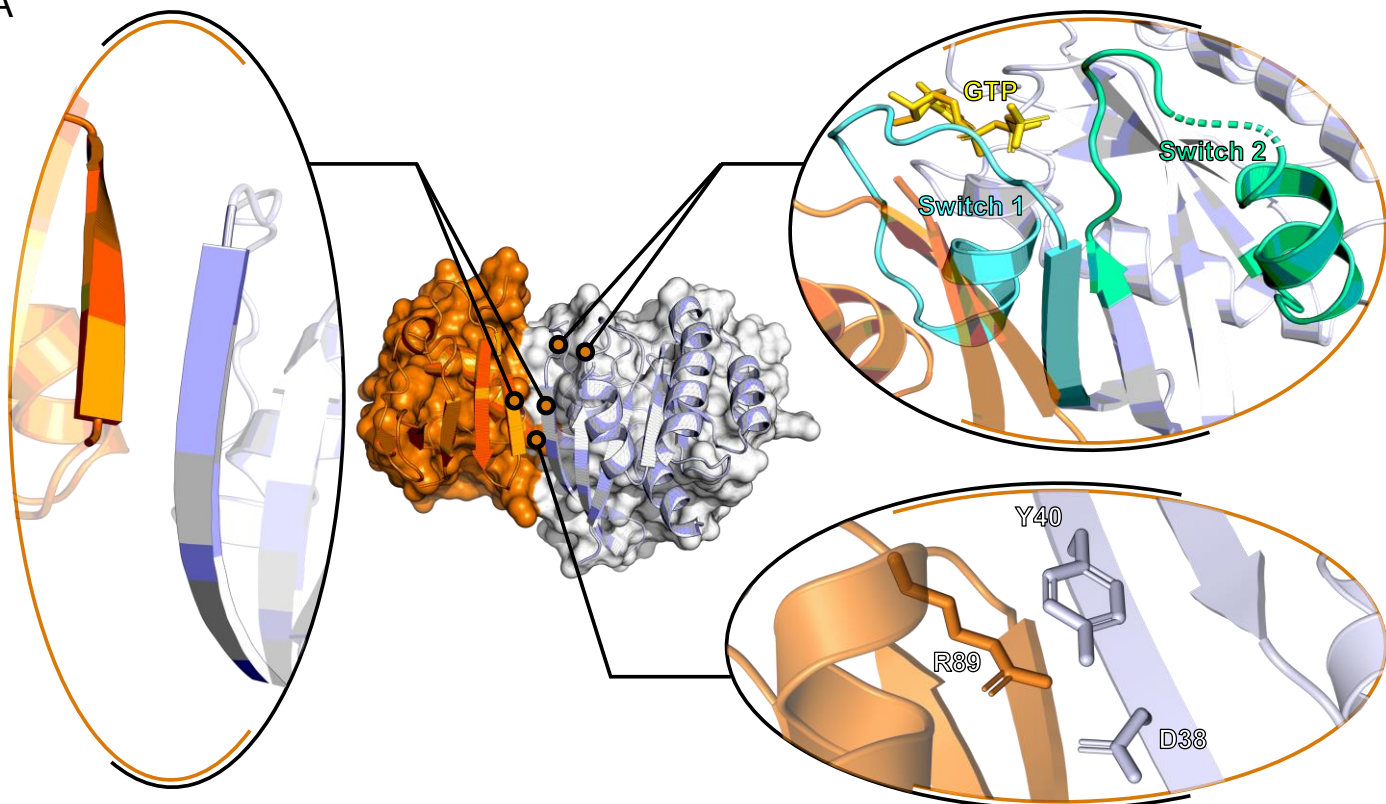
- 642 1. R. Gasper, F. Wittinghofer, The Ras switch in structural and historical perspective. *Biol Chem*
643 **401**, 143-163 (2019).
- 644 2. E. F. Pai *et al.*, Structure of the guanine-nucleotide-binding domain of the Ha-ras oncogene
645 product p21 in the triphosphate conformation. *Nature* **341**, 209-214 (1989).
- 646 3. E. F. Pai *et al.*, Refined crystal structure of the triphosphate conformation of H-ras p21 at 1.35
647 Å resolution: implications for the mechanism of GTP hydrolysis. *Embo j* **9**, 2351-2359 (1990).
- 648 4. C. Kiel, L. Serrano, The ubiquitin domain superfold: structure-based sequence alignments and
649 characterization of binding epitopes. *J Mol Biol* **355**, 821-844 (2006).
- 650 5. D. K. Simanshu, D. V. Nissley, F. McCormick, RAS Proteins and Their Regulators in Human
651 Disease. *Cell* **170**, 17-33 (2017).
- 652 6. V. Ibáñez Gaspar, S. Catozzi, C. Ternet, P. J. Luthert, C. Kiel, Analysis of Ras-effector
653 interaction competition in large intestine and colorectal cancer context. *Small GTPases* **12**,
654 209-225 (2021).
- 655 7. S. Catozzi, M. Halasz, C. Kiel, Predicted 'wiring landscape' of Ras-effector interactions in 29
656 human tissues. *NPJ Syst Biol Appl* **7**, 10 (2021).
- 657 8. C. Kiel, D. Matallanas, W. Kolch, The Ins and Outs of RAS Effector Complexes. *Biomolecules*
658 **11**, (2021).
- 659 9. S. Catozzi *et al.*, Reconstruction and analysis of a large-scale binary Ras-effector signaling
660 network. *Cell Commun Signal* **20**, 24 (2022).
- 661 10. C. Kiel, E. Verschuere, J. S. Yang, L. Serrano, Integration of protein abundance and structure
662 data reveals competition in the ErbB signaling network. *Sci Signal* **6**, ra109 (2013).
- 663 11. B. N. Kholodenko, J. B. Hoek, H. V. Westerhoff, Why cytoplasmic signalling proteins should be
664 recruited to cell membranes. *Trends Cell Biol* **10**, 173-178 (2000).
- 665 12. C. Kiel, M. Foglierini, N. Kuemmerer, P. Beltrao, L. Serrano, A genome-wide Ras-effector
666 interaction network. *J Mol Biol* **370**, 1020-1032 (2007).
- 667 13. C. Kiel, L. Serrano, Prediction of Ras-effector interactions using position energy matrices.
668 *Bioinformatics* **23**, 2226-2230 (2007).
- 669 14. J. Jumper *et al.*, Highly accurate protein structure prediction with AlphaFold. *Nature* **596**,
670 583-589 (2021).
- 671 15. M. Varadi *et al.*, AlphaFold Protein Structure Database: massively expanding the structural
672 coverage of protein-sequence space with high-accuracy models. *Nucleic Acids Res* **50**, D439-
673 d444 (2022).
- 674 16. R. C. Gimple, X. Wang, RAS: Striking at the Core of the Oncogenic Circuitry. *Front Oncol* **9**, 965
675 (2019).
- 676 17. A. R. Moore, S. C. Rosenberg, F. McCormick, S. Malek, RAS-targeted therapies: is the
677 undruggable drugged? *Nat Rev Drug Discov* **19**, 533-552 (2020).
- 678 18. A. G. Stephen, D. Esposito, R. K. Bagni, F. McCormick, Dragging ras back in the ring. *Cancer*
679 *Cell* **25**, 272-281 (2014).
- 680 19. Q. Zhong *et al.*, Edgetic perturbation models of human inherited disorders. *Mol Syst Biol* **5**,
681 321 (2009).
- 682 20. C. Kiel, L. Serrano, Structure-energy-based predictions and network modelling of RASopathy
683 and cancer missense mutations. *Mol Syst Biol* **10**, 727 (2014).
- 684 21. P. Junk, C. Kiel, Engineering of Biological Pathways: Complex Formation and Signal
685 Transduction. *Methods Mol Biol* **2315**, 59-70 (2021).
- 686 22. P. Junk, C. Kiel, HOMELETTE: a unified interface to homology modelling software.
687 *Bioinformatics* **38**, 1749-1751 (2021).
- 688 23. I. Jarmoskaite, I. AlSadhan, P. P. Vaidyanathan, D. Herschlag, How to measure and evaluate
689 binding affinities. *Elife* **9**, (2020).
- 690 24. J. Schymkowitz *et al.*, The FoldX web server: an online force field. *Nucleic Acids Res* **33**,
691 W382-388 (2005).

- 692 25. I. R. Humphreys *et al.*, Computed structures of core eukaryotic protein complexes. *Science*
693 **374**, eabm4805 (2021).
- 694 26. A. F. Citalán-Madrid, A. García-Ponce, H. Vargas-Robles, A. Betanzos, M. Schnoor, Small
695 GTPases of the Ras superfamily regulate intestinal epithelial homeostasis and barrier
696 function via common and unique mechanisms. *Tissue Barriers* **1**, e26938 (2013).
- 697 27. T. A. Martin, W. G. Jiang, Loss of tight junction barrier function and its role in cancer
698 metastasis. *Biochim Biophys Acta* **1788**, 872-891 (2009).
- 699 28. B. H. Choi *et al.*, Identification of Radil as a Ras binding partner and putative activator. *J Biol*
700 *Chem* **296**, 100314 (2021).
- 701 29. S. P. Zimmerman, C. L. Hueschen, D. Malide, S. L. Milgram, M. P. Playford, Sorting nexin 27
702 (SNX27) associates with zonula occludens-2 (ZO-2) and modulates the epithelial tight
703 junction. *Biochem J* **455**, 95-106 (2013).
- 704 30. X. H. Zhou *et al.*, RASSF5 inhibits growth and invasion and induces apoptosis in osteosarcoma
705 cells through activation of MST1/LATS1 signaling. *Oncol Rep* **32**, 1505-1512 (2014).
- 706 31. V. B. Chen *et al.*, MolProbity: all-atom structure validation for macromolecular
707 crystallography. *Acta Crystallogr D Biol Crystallogr* **66**, 12-21 (2010).
- 708 32. C. J. Williams *et al.*, MolProbity: More and better reference data for improved all-atom
709 structure validation. *Protein Sci* **27**, 293-315 (2018).
- 710 33. R. Guerois, J. E. Nielsen, L. Serrano, Predicting changes in the stability of proteins and protein
711 complexes: a study of more than 1000 mutations. *J Mol Biol* **320**, 369-387 (2002).
- 712 34. C. Kiel, L. Serrano, C. Herrmann, A detailed thermodynamic analysis of ras/effector complex
713 interfaces. *J Mol Biol* **340**, 1039-1058 (2004).
- 714 35. C. Kiel, L. Serrano, Cell type-specific importance of ras-c-raf complex association rate
715 constants for MAPK signaling. *Sci Signal* **2**, ra38 (2009).
- 716 36. I. R. Vetter, A. Wittinghofer, The guanine nucleotide-binding switch in three dimensions.
717 *Science* **294**, 1299-1304 (2001).
- 718 37. Y. Zhang, J. Skolnick, TM-align: a protein structure alignment algorithm based on the TM-
719 score. *Nucleic Acids Res* **33**, 2302-2309 (2005).
- 720 38. J. Mistry *et al.*, Pfam: The protein families database in 2021. *Nucleic Acids Res* **49**, D412-d419
721 (2021).
- 722 39. UniProt: the universal protein knowledgebase in 2021. *Nucleic Acids Res* **49**, D480-d489
723 (2021).
- 724 40. M. Mirdita *et al.*, ColabFold: making protein folding accessible to all. *Nat Methods* **19**, 679-
725 682 (2022).
- 726 41. R. Evans *et al.*, (2022).
- 727 42. M. Mirdita, M. Steinegger, J. Söding, MMseqs2 desktop and local web server app for fast,
728 interactive sequence searches. *Bioinformatics* **35**, 2856-2858 (2019).
- 729 43. M. Mirdita *et al.*, Uniclust databases of clustered and deeply annotated protein sequences
730 and alignments. *Nucleic Acids Res* **45**, D170-d176 (2017).
- 731 44. A. L. Mitchell *et al.*, MGnify: the microbiome analysis resource in 2020. *Nucleic Acids Res* **48**,
732 D570-d578 (2020).
- 733 45. M. Steinegger *et al.*, HH-suite3 for fast remote homology detection and deep protein
734 annotation. *BMC Bioinformatics* **20**, 473 (2019).
- 735 46. H. Berman, K. Henrick, H. Nakamura, Announcing the worldwide Protein Data Bank. *Nat*
736 *Struct Biol* **10**, 980 (2003).
- 737 47. P. Eastman *et al.*, OpenMM 7: Rapid development of high performance algorithms for
738 molecular dynamics. *PLoS Comput Biol* **13**, e1005659 (2017).
- 739 48. A. Sali, T. L. Blundell, Comparative protein modelling by satisfaction of spatial restraints. *J*
740 *Mol Biol* **234**, 779-815 (1993).
- 741 49. B. Webb, A. Sali, Comparative Protein Structure Modeling Using MODELLER. *Curr Protoc*
742 *Bioinformatics* **54**, 5.6.1-5.6.37 (2016).

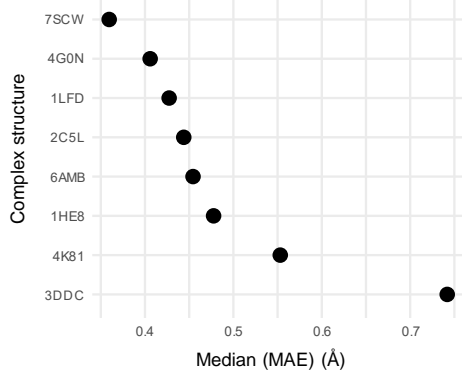
- 743 50. G. Janson *et al.*, Revisiting the "satisfaction of spatial restraints" approach of MODELLER for
744 protein homology modeling. *PLoS Comput Biol* **15**, e1007219 (2019).
- 745 51. P. Benkert, S. C. Tosatto, D. Schomburg, QMEAN: A comprehensive scoring function for
746 model quality assessment. *Proteins* **71**, 261-277 (2008).
- 747 52. P. Benkert, M. Biasini, T. Schwede, Toward the estimation of the absolute quality of
748 individual protein structure models. *Bioinformatics* **27**, 343-350 (2011).
- 749 53. G. Q. Dong, H. Fan, D. Schneidman-Duhovny, B. Webb, A. Sali, Optimized atomic statistical
750 potentials: assessment of protein interfaces and loops. *Bioinformatics* **29**, 3158-3166 (2013).
- 751 54. M. Ankerst, M. M. Breunig, H.-P. Kriegel, J. Sander, Optics. *ACM SIGMOD Record* **28**, 49-60
752 (1999).
- 753 55. D. Wang *et al.*, A deep proteome and transcriptome abundance atlas of 29 healthy human
754 tissues. *Mol Syst Biol* **15**, e8503 (2019).
- 755 56. S. Rezaei Adariani *et al.*, A comprehensive analysis of RAS-effector interactions reveals
756 interaction hotspots and new binding partners. *J Biol Chem* **296**, 100626 (2021).
- 757 57. M. W. Dorrity, L. M. Saunders, C. Queitsch, S. Fields, C. Trapnell, Dimensionality reduction by
758 UMAP to visualize physical and genetic interactions. *Nat Commun* **11**, 1537 (2020).
- 759

Figure 1

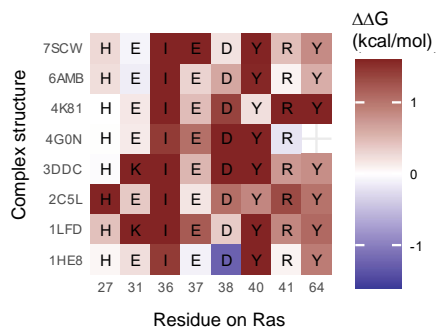
A



B



C



D

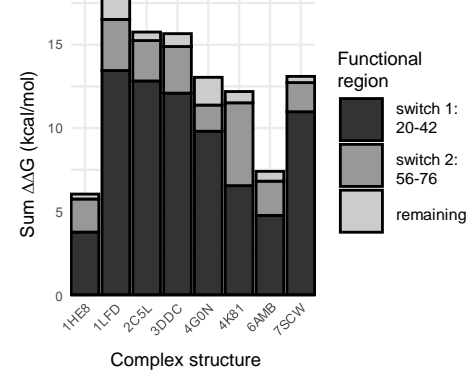


Figure 2

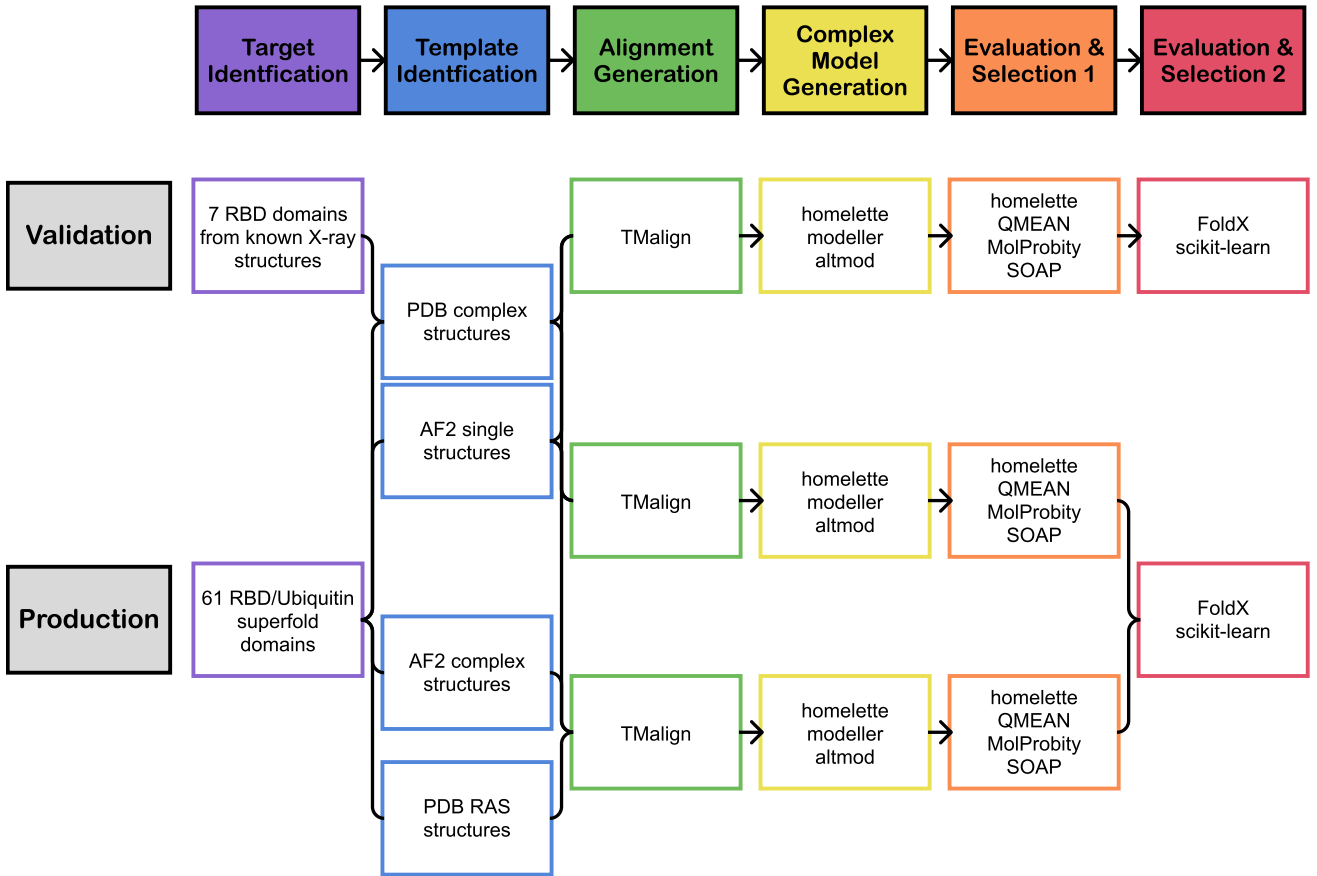


Figure 3

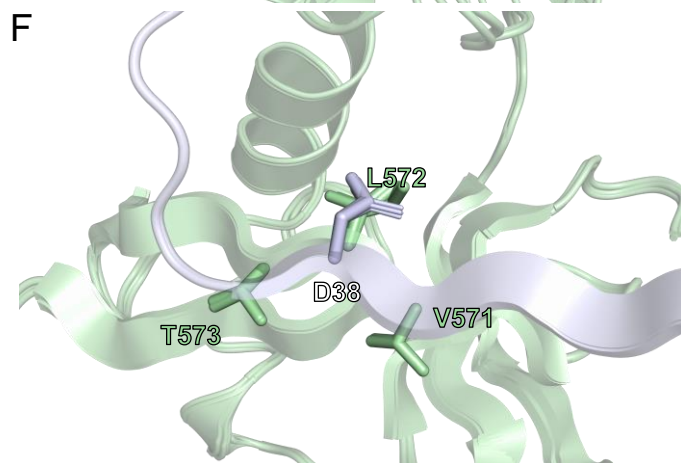
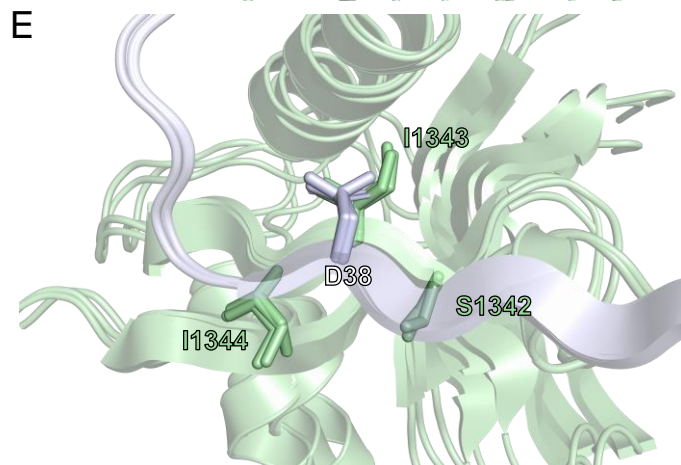
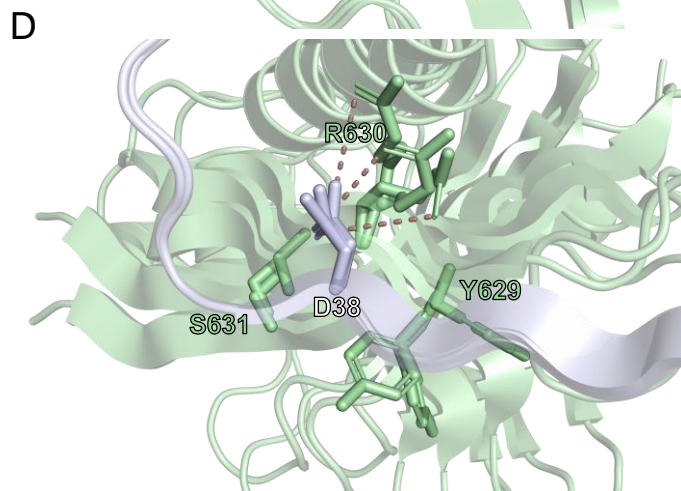
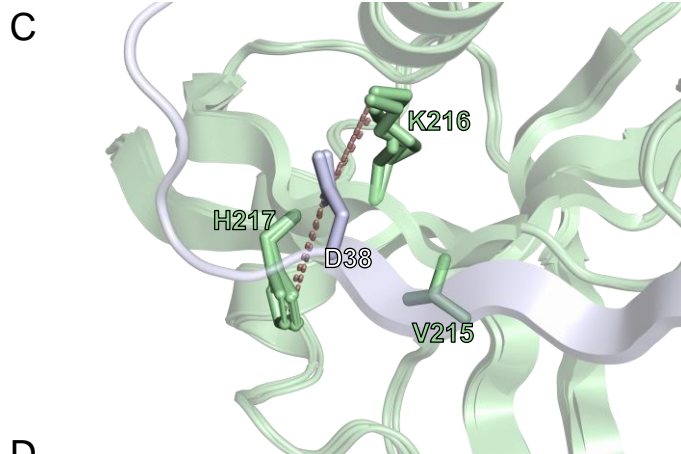
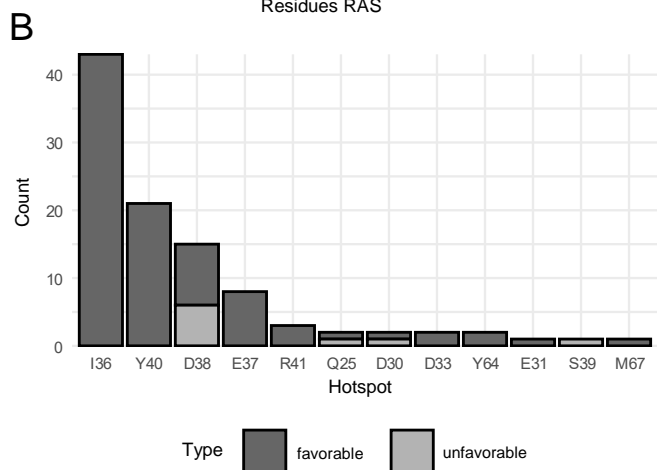
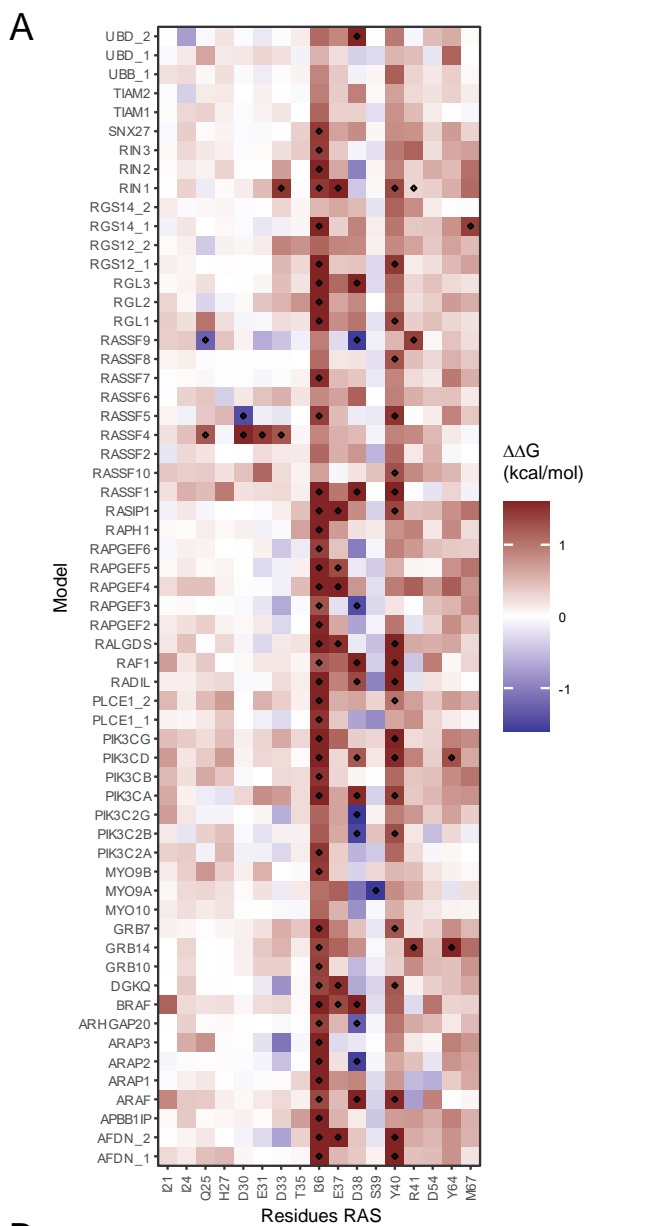


Figure 4

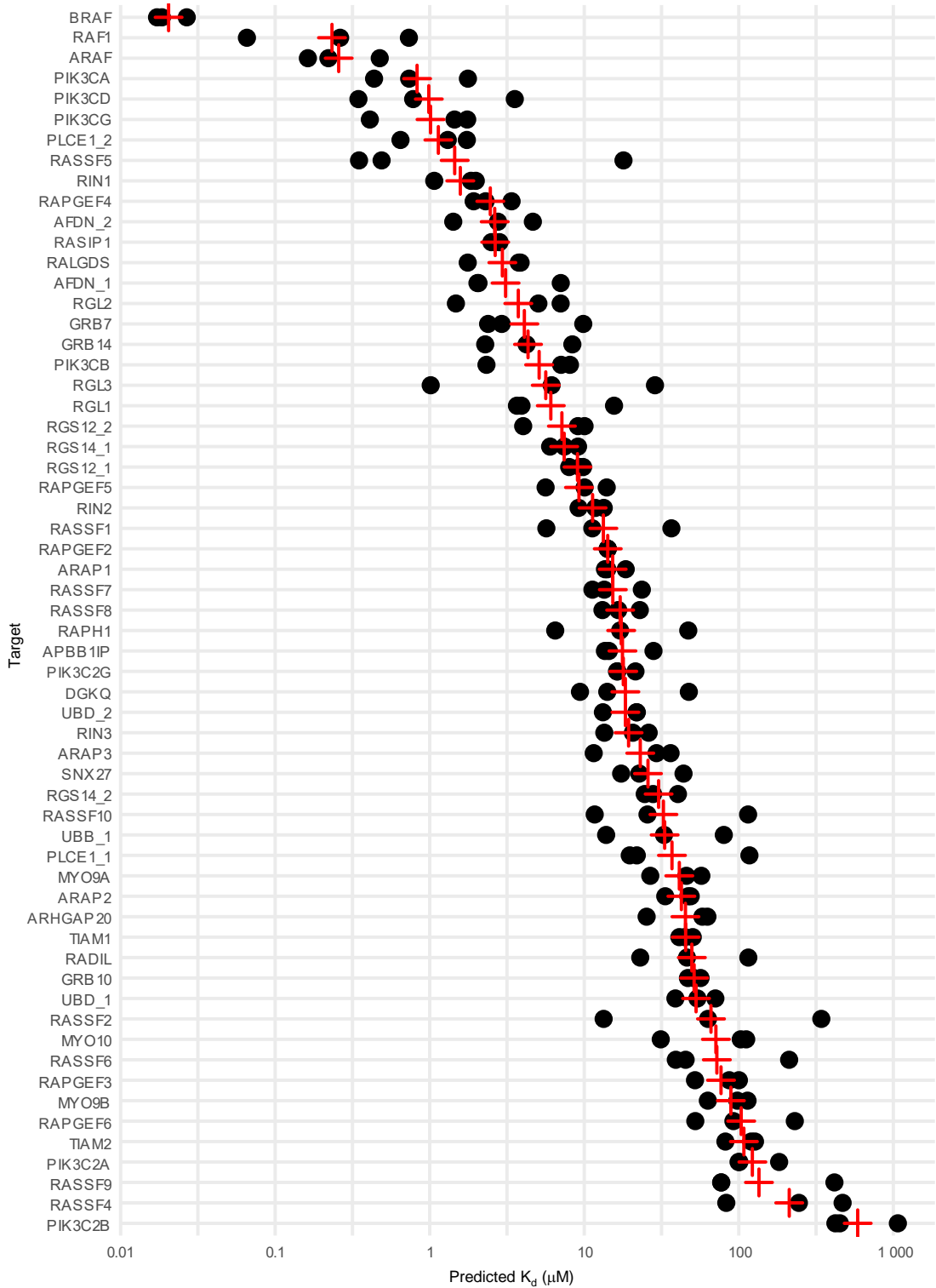


Figure 5

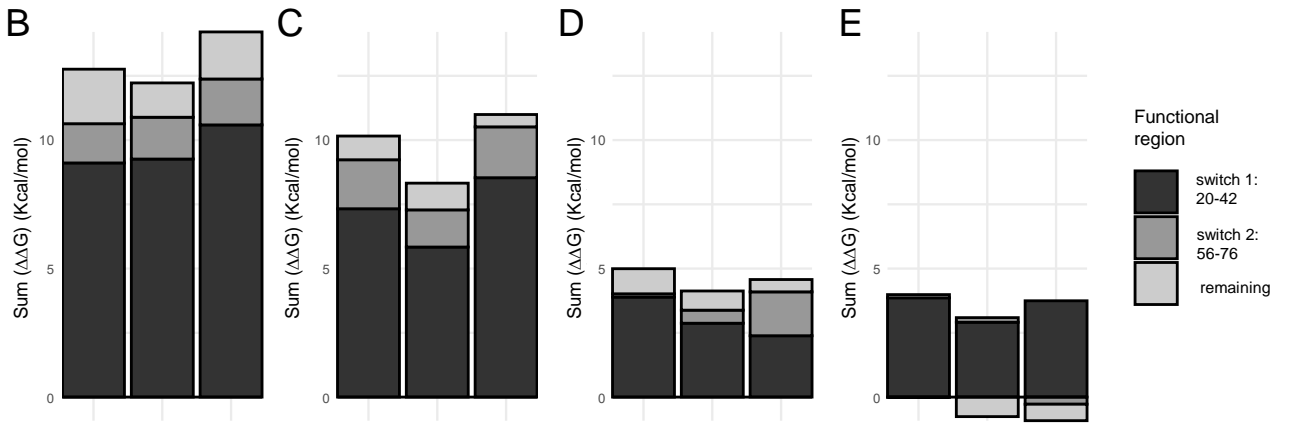
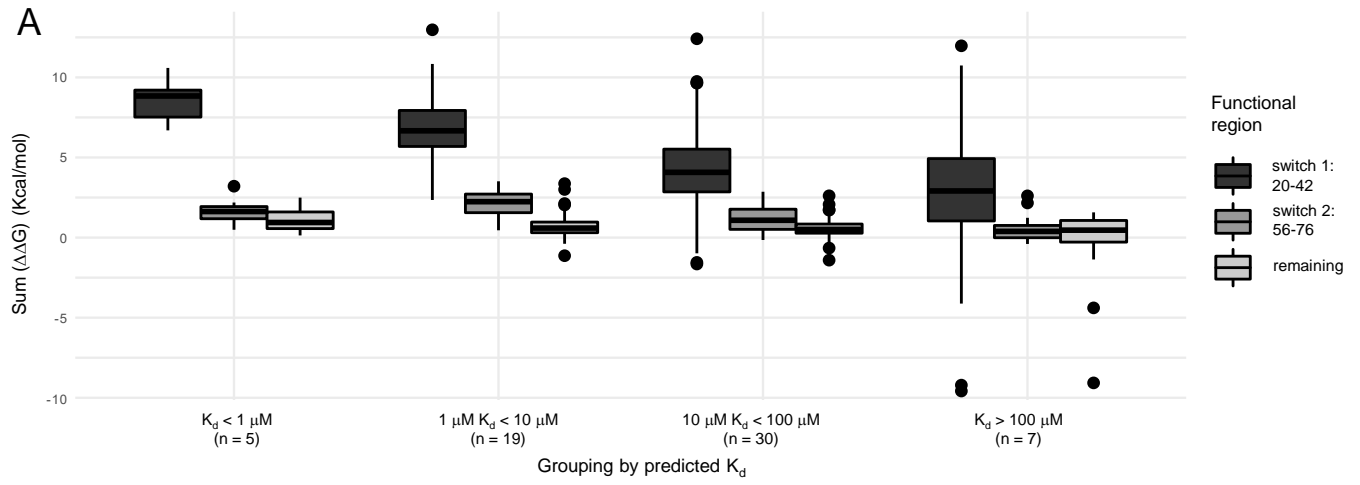


Figure 6

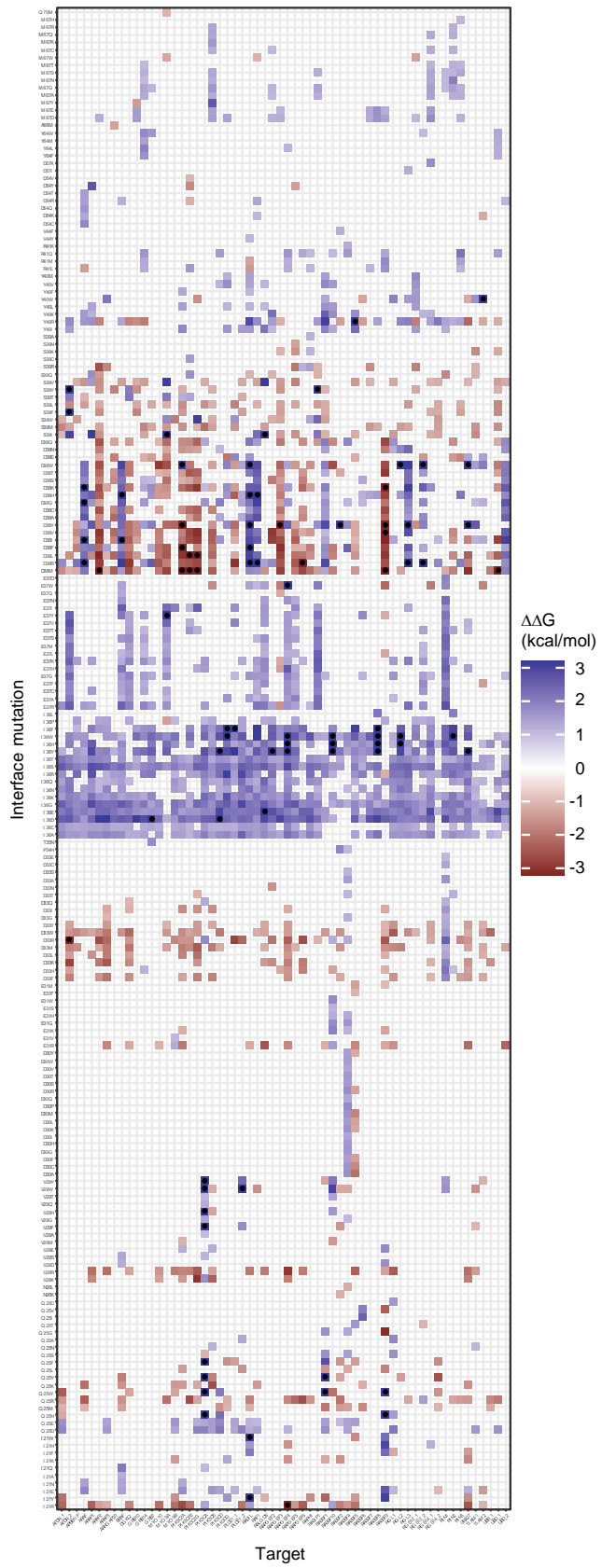
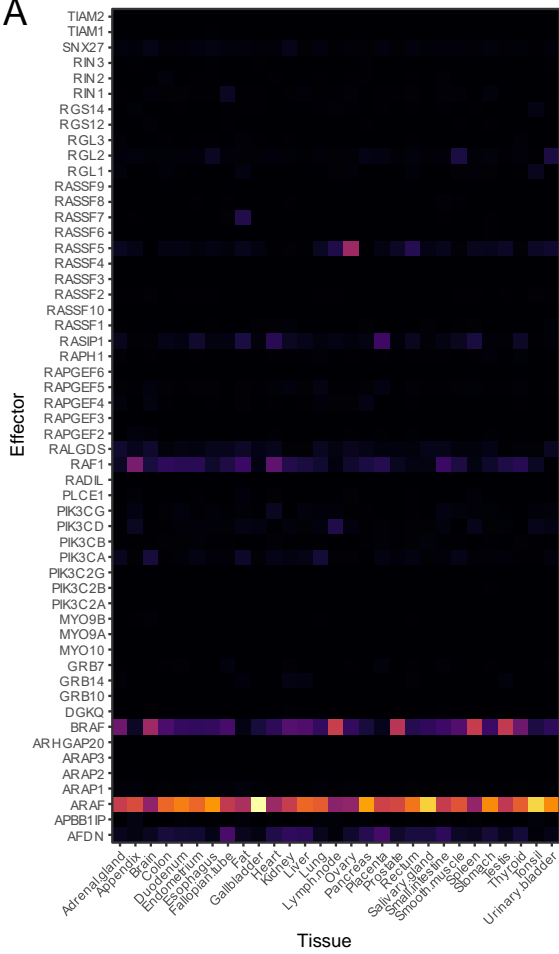
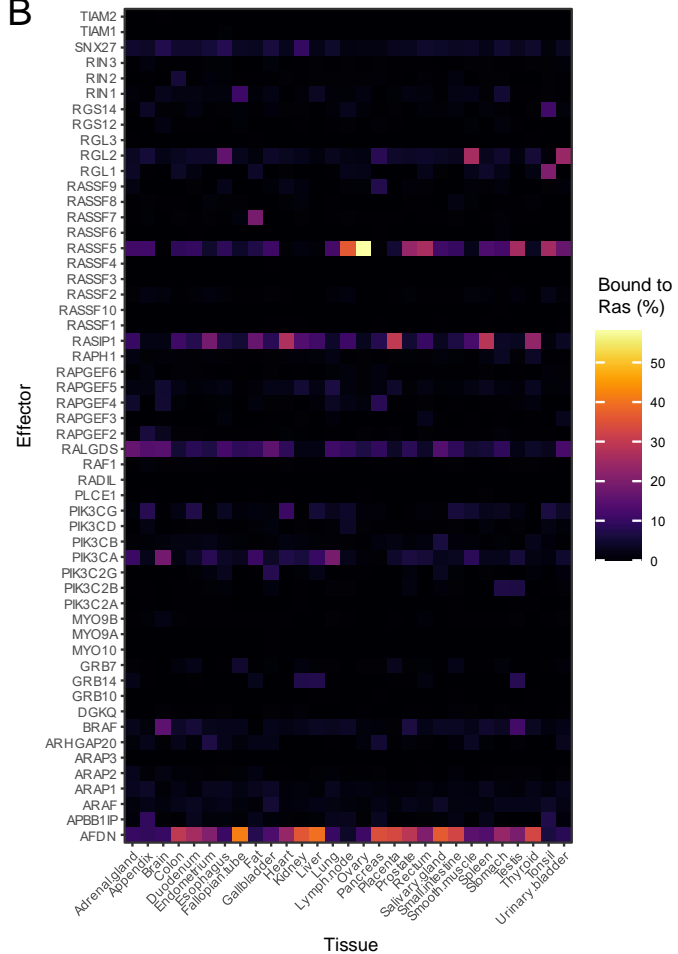


Figure 7

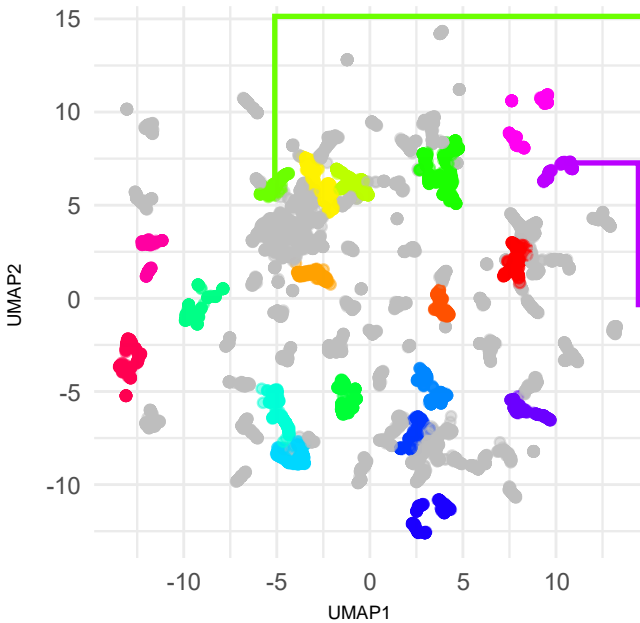
A



B



C



D

